

# The Máni mission

Hugo Lancery, Frederic Schmidt

December 16, 2024

## Abstract

Ours principals objectives in the Máni mission are the prototyping and investigation of photometric scenarios in order to better characterize the geological processes of the Moon. We will study over N areas scattered across the surface and estimated their photometric behaviour using the Hapke radiative transfer model and [mc3](#) inversion in order to estimate their microphysical state. The mission consist in a multiple passby orbit over the targeted aeras, with an altitude of 50 km.



# Contents

<b>1</b>	<b>Context, objectives and challenges of characterizing optimal orbital geometries.</b>	<b>5</b>
1.1	Generalities . . . . .	5
1.2	Moon's surface properties . . . . .	6
1.3	Objectives . . . . .	6
<b>2</b>	<b>Creation of multiples orbital geometric scenarios</b>	<b>7</b>
2.1	Definition of the geometric parameters . . . . .	7
2.1.1	Orbital geometric scenarios . . . . .	8
2.2	Calulus of geometric angles . . . . .	11
2.2.1	Combination of orbit . . . . .	13
<b>3</b>	<b>Creation of multiples set of photometric parameters</b>	<b>14</b>
3.1	Surface photometry . . . . .	14
3.2	Photometric parameters configurations . . . . .	15
3.2.1	Reflectance calculus . . . . .	15
<b>4</b>	<b>Reflectance inversion to estimate photometric parameters</b>	<b>16</b>
4.1	inversion method . . . . .	16
4.1.1	Estimation of the geometric configuration quality . . . . .	18
<b>5</b>	<b>Results</b>	<b>19</b>
5.1	Results on one orbit . . . . .	19
5.2	Results on combination of orbit . . . . .	20
5.3	Effect of the noise level . . . . .	23

# Introduction

Understanding the geological processes that shape the surface of the Moon is a key objective for lunar exploration, as it provides insights into the Moon’s history and evolution. The Máni mission aims to advance this understanding by characterizing the lunar regolith with high resolution imagery, high resolution Digital Elevation Model (DEM) and photometry. The aim of this project is to prototype the mission and investigating photometric scenarios to characterize the lunar surface in greater detail. Specifically, the mission will focus on studying the photometric behavior of lunar areas across multiple regions, leveraging advanced models to estimate their microphysical properties.

At the core of this investigation is the use of the Hapke radiative transfer model, a widely accepted approach for interpreting the interaction of light with planetary surfaces proposed by [Sat14]. Through the application of the MC3 [Cub+17] inversion tool, we will quantify the surface properties that govern the scattering and absorption of light, allowing us to infer crucial details about the mineralogy, texture, and physical state of the lunar regolith.

The Máni mission will employ a multiple-pass polar orbit strategy, flying at an altitude of 50 km above the targeted regions. This orbital configuration allows for high-resolution observations and repeated measurements across a variety of lunar terrains, ensuring a comprehensive assessment of the photometric characteristics. The data collected will contribute to a deeper understanding of lunar geology and support the broader goals of lunar exploration, including future manned missions and resource utilization.

This report details the methodology, objectives, and expected outcomes of the Máni mission, setting the stage for a thorough exploration of the Moon’s surface through the lens of photometric analysis.

## Nomenclature

Symbol	Description
$\omega$	Single scattering albedo: Ratio of scattering efficiency to total light extinction
$\zeta$	Hapke mean slope roughness parameter
$B_0$	Opposition effect amplitude: Describes intensity of opposition effect
$b$	Asymmetry parameter: Describes angular distribution of scattered light
$c$	Backscatter fraction: Related to backward scattering lobe in phase function
$h$	Opposition effect width: Width of the opposition effect
$\theta_0$	Incidence angle: $\angle LCT$ between light source and surface normal (target)
$\theta$	Emergence angle: $\angle OCT$ between observer and surface normal (target)
$\alpha$	Phase angle: $\angle LCO$ between light source and observer direction
$\psi$	Azimuth angle: $\angle L'TO'$ between light source and observer projection
$C$	Center of the Moon
$L$	Subsolar point on the Moon
$T$	Target point on the Moon surface
$O$	Observer point in orbit
$L'$	$L$ projection on the perpendicular plane of the $\vec{CL}$ vector
$O'$	$O$ projection on the perpendicular plane of the $\vec{TO}$ vector

# 1 Context, objectives and challenges of characterizing optimal orbital geometries.

## 1.1 Generalities

The Moon<sup>1</sup> Figure 1 is the only natural satellite of the Earth and is located at an average distance of 384,400 km from our planet. It completes its revolution around the Earth in approximately 27.3 days and exhibits synchronous rotation, always showing the same face to the Earth. With a mean radius of 1,737 km, the Moon is about 3.7 times smaller than the Earth in diameter. Its average density is  $3.34 \text{ g.cm}^3$ , and its gravity is  $1.62 \text{ m.s}^{-2}$ , approximately 0.17 times that of Earth.



Figure 1: The Moon (Credit: NASA)

The Moon does not have a significant atmosphere but instead has an extremely tenuous exosphere<sup>2</sup>, composed primarily of hydrogen, neon, and helium atoms. Due to the absence of a dense atmosphere, the Moon cannot sustain a greenhouse effect, resulting in extreme temperature contrasts between illuminated and shadowed regions. Surface temperatures range from  $-173^\circ\text{C}$  during the lunar night to  $127^\circ\text{C}$  during the day, illustrating a particularly harsh environment.

The lunar surface is covered by regolith, a layer of fine particles formed by billions of years of meteoritic bombardment and space weathering processes. This regolith varies in thickness across the surface, reaching depths of several meters in the plains. It consists of rock fragments, glass particles, and mineral grains derived from the lunar crust.

Although the Moon does not exhibit current tectonic activity, it features remarkable geological characteristics such as lunar maria (dark basaltic plains formed by ancient lava flows) and highlands (bright areas rich in anorthosite). These features indicate past volcanic activity that ceased approximately 1 billion years ago. Impact craters, scattered across the Moon's surface, provide a valuable record of events in the solar system since the Moon's formation about 4.5 billion years ago.

Finally, discoveries from the Apollo missions and recent robotic explorations have identified deposits of ice within permanently shadowed regions near the lunar poles<sup>3</sup>. These polar regions, with consistently low temperatures, are of critical importance for future human exploration and hold scientific value for studying volatiles and the Moon's thermal history. The following sections delve into the morphological and physicochemical properties of the lunar surface and their significance in the context of photometric studies.

---

<sup>1</sup>NASA: <https://nssdc.gsfc.nasa.gov/planetary/factsheet/moonfact.html>

<sup>2</sup>NASA: <https://www.nasa.gov/general/is-there-weather-on-the-moon-we-asked-a-nasa-scientist-episode-34/>

<sup>3</sup>NASA: <https://science.nasa.gov/solar-system/moon/nasas-lro-lunar-ice-deposits-are-widespread/>

## 1.2 Moon's surface properties

The Moon's surface exhibits distinct morphological and physicochemical characteristics that play a crucial role in photometric studies. These properties influence how light interacts with the surface and determine the variations in observed reflectance.

The lunar surface is characterized by two primary terrains: the highlands, composed of anorthositic rocks with high albedo, and the maria, basaltic plains with lower albedo. These features, combined with impact craters and the fine-grained regolith, create a complex morphology that influences the scattering of sunlight. The mineral composition, primarily composed of silicates such as plagioclase, pyroxene, and olivine, affects reflectance properties. Space weathering, including micrometeorite impacts and solar wind exposure, alters the surface by forming nanophase iron particles, which darken and reduce reflectance over time.

In photometric studies, these properties are essential for modeling the interaction of light with the surface. One key parameter is the bidirectional reflectance distribution function (BRDF), which quantifies how light is reflected at an interface as a function of the illumination and viewing angles. The BRDF is critical for interpreting remote sensing data, mapping compositional variations, and understanding the Moon's geological history. Accurate photometric analysis should also support exploration planning and the identification of regions with potential ice deposits.

## 1.3 Objectives

The primary objective of my work has been to identify and study various orbital configurations to determine which are best suited for accurately characterizing the photometric properties of the lunar surface. By simulating and analyzing different orbital geometries, this study aims to assess how factors such as inclination, altitude, and latitude impact the quality and reliability of reflectance data.

The goal is to optimize orbital parameters to maximize coverage of diverse lunar terrains, including highlands, maria, and regions near the poles, while ensuring robust data collection under varying illumination and observational conditions. This evaluation is critical for improving the precision of photometric models, advancing our understanding of the Moon's surface properties, and supporting future exploration missions.

## 2 Creation of multiples orbital geometric scenarios

### 2.1 Definition of the geometric parameters

In the Máni mission scenario, a satellite conducts multiple passes around specific target regions on the Moon's surface to gather photometric data from various angles.

We assume here the Moon as a perfect sphere, without slope. The left side of the [Figure 2](#) represents a global view, showing the Moon with latitude and longitude coordinates marked. Here, the yellow star symbol (L, for light source) represents the subsolar point of the Sun on the surface, while the green circle symbol (O, for observer) represents the observer point, which is the location of the satellite and the red circle symbol (T, for target) shows the target position.

The angle  $(\vec{n}, \vec{CL})$  denotes the incidence angle, which is the angle between the normal vector  $\vec{n}$  to the surface and the incoming sunlight. The emergence angle  $(\vec{n}, \vec{TO})$  is the angle between  $\vec{n}$  and the line of sight from the satellite.

The right side of the image provides a more detailed, localized view of a specific target area on the Moon's surface, indicated by the point (T). Here, the orientation of the normal vector  $\vec{n}$  to the surface is highlighted, along with several critical angles that are essential to the photometric analysis. The angle  $(\vec{CL}, \vec{TO})$  represents the phase angle, which is the angle between the direction of the incoming sunlight and the observer's line of sight.  $(\vec{TL'}, \vec{TO'})$  is the relative azimuth angle, defining the orientation of the satellite's view relative to the local coordinate frame on the surface.

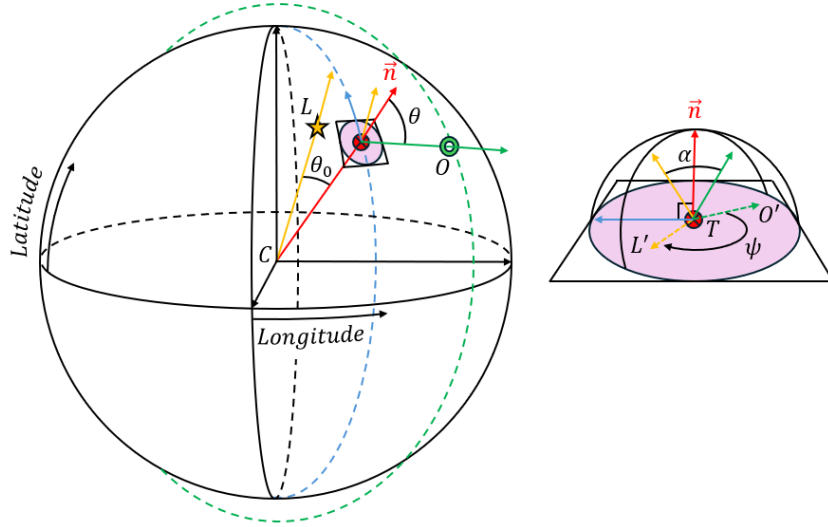


Figure 2: Graph representing the system coordinates and geometries used for a given scenario, the left figure represents the global configuration view with the incidence, emergence angles and the Target, Light and Observer points. The right figure represents a zoom on the normal plan from the target normal vector  $\vec{n}$  with the azimuth and phase angle

### 2.1.1 Orbital geometric scenarios

We selected scenarios with diversified Targets across the equator, medium, and high latitudes to evaluate later its impact on the reflectance and the inversion of the reflectance to predict photometric parameters. Therefore, to cover all possibility we made the following 15 scenarios.

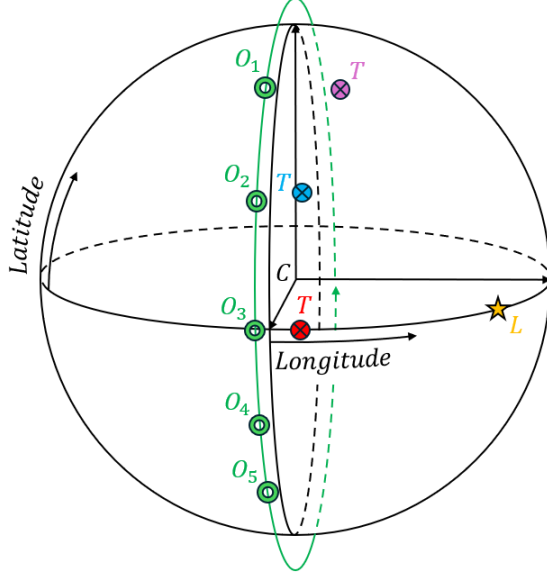


Figure 3: Scenarios graph of  $E_1$ ,  $M_1$ ,  $H_1$

This geometric configuration in Figure 3, has 5 Observer points along a polar orbit at longitude  $0^\circ$  called  $O_i$  corresponding to each shot taken during the pass-by of the satellite. First, a condition on the emergence was applied restricting its value under  $80^\circ$ . Second, we keep the first, last, and middle points of the emergence range. Third, we take the in-between values of the first and second half. The Observer is initialized in the same way for each configuration in Python with a given latitude range from  $-180^\circ$  to  $180^\circ$ . For this scenario, the subsolar point  $L$  was placed at a high longitude on the equator. The Target points  $T$ ,  $T$ ,  $T$  for this first configuration are spread out on the equator, medium, and high latitude.

	$lon^\circ, lat^\circ$	$lon^\circ, lat^\circ$	$lat_0^\circ, lat_{-1}^\circ$
	<b>T</b>	<b>L</b>	<b>O</b>
<b>E1</b>	(5, 0)	(70, 0)	(-180, 180)
<b>M1</b>	(5, 45)	(70, 0)	(-180, 180)
<b>H1</b>	(10, 70)	(70, 0)	(-180, 180)

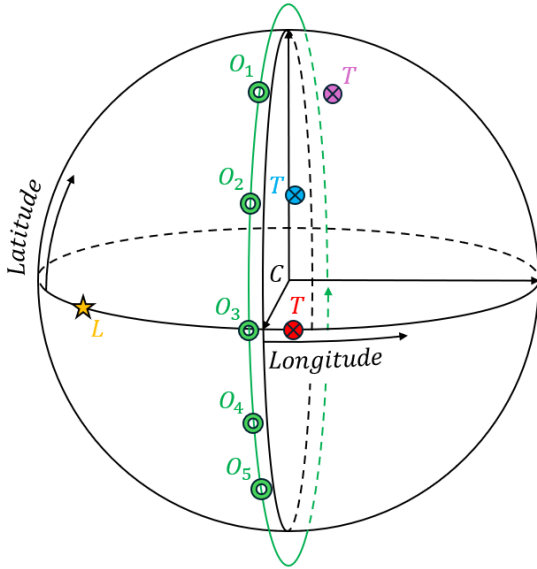


Figure 4: Scenarios graph of  $E_2$ ,  $M_2$ ,  $H_2$

This second scenario in Figure 4, has the same configuration as the Figure 3 except for the subsolar point  $L$ , placed at a high negative longitude on the equator.

	$lon^\circ, lat^\circ$	$lon^\circ, lat^\circ$	$lat_0^\circ, lat_{-1}^\circ$
	<b>T</b>	<b>L</b>	<b>O</b>
<b>E2</b>	(5, 0)	(-70, 0)	(-180, 180)
<b>M2</b>	(5, 45)	(-70, 0)	(-180, 180)
<b>H2</b>	(10, 70)	(-70, 0)	(-180, 180)



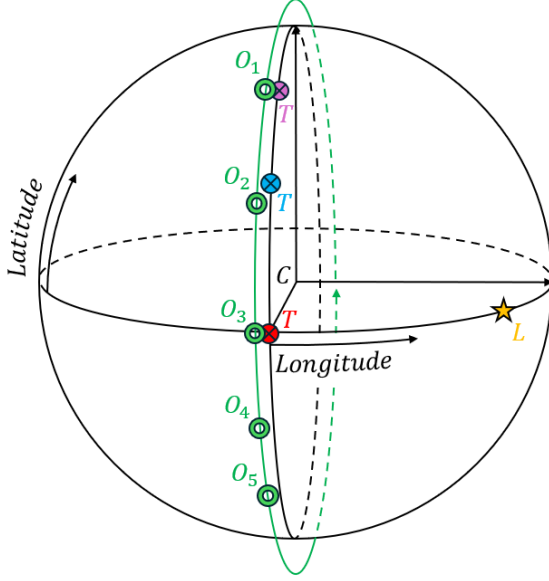


Figure 5: Scenarios graph of  $E_3$ ,  $M_3$ ,  $H_3$

This third scenario in Figure 5, has the same configuration as the Figure 3 except for the Target points  $T$ ,  $T$ ,  $T$  placed along the longitude  $0^\circ$ .

	$lon^\circ, lat^\circ$	$lon^\circ, lat^\circ$	$lat_0^\circ, lat_{-1}^\circ$
	<b>T</b>	<b>L</b>	<b>O</b>
<b>E3</b>	(0, 0)	(70, 0)	(-180, 180)
<b>M3</b>	(0, 45)	(70, 0)	(-180, 180)
<b>H3</b>	(0, 70)	(70, 0)	(-180, 180)

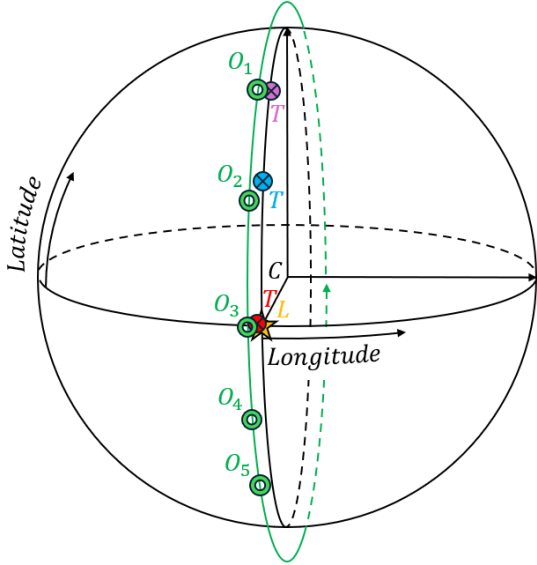


Figure 6: Scenarios graph of  $E_4$ ,  $M_4$ ,  $H_4$

This fourth scenario in Figure 6, has the same configuration as the Figure 5 except for the subsolar point  $L$ , placed at nadir.

	$lon^\circ, lat^\circ$	$lon^\circ, lat^\circ$	$lat_0^\circ, lat_{-1}^\circ$
	<b>T</b>	<b>L</b>	<b>O</b>
<b>E4</b>	(0, 0)	(0, 0)	(-180, 180)
<b>M4</b>	(0, 45)	(0, 0)	(-180, 180)
<b>H4</b>	(0, 70)	(0, 0)	(-180, 180)



## 2.2 Calulus of geometric angles

For each of the defined Sun-target-observer combinations from [Table 1](#), the calculation of the photometric angles of incidence ( $\theta_0$ ), emergence ( $\theta$ ), phase ( $\alpha$ ), and azimuth ( $\psi$ ) were performed. These angles are essential for characterizing the interaction of light with the lunar surface and are derived using vector geometry in the Moon's reference frame as described in the [subsection 2.1](#).

- Incidence ( $\theta_0$ ): The angle between the surface normal at the target point and the vector pointing from the target to the Sun. It is calculated using the scalar product:

$$\theta_0 = \arccos\left(\frac{\vec{CL} \cdot \vec{CT}}{\|\vec{CL}\| \cdot \|\vec{CT}\|}\right)$$

- Emergence ( $\theta$ ): The angle between the surface normal at the target point and the vector pointing from the target to the observer. However, the vector  $\vec{CO}$  can be approximated to  $\vec{TO}$  due to the distance Earth-Sun. It provides information on the observer's line of sight relative to the surface normal and is determined by:

$$\theta = \arccos\left(\frac{\vec{CT} \cdot \vec{TO}}{\|\vec{CT}\| \cdot \|\vec{TO}\|}\right)$$

- Phase ( $\alpha$ ): The angle between the vector pointing from the target to the observer and the vector pointing from the target to the Sun. This angle determines the relative Sun-observer-target geometry and is calculated as:

$$\alpha = \arccos\left(\frac{\vec{CL} \cdot \vec{TO}}{\|\vec{CL}\| \cdot \|\vec{TO}\|}\right)$$

- Azimuth ( $\psi$ ): The azimuth is the angle between the projection of the Sun vector and the observer vector onto the local horizontal plane at the target point. It describes the relative orientation of the Sun and observer in the plane tangential to the surface:

$$T_{\perp} = \frac{\vec{CT}}{\|\vec{CT}\|} \times \frac{\vec{TO}}{\|\vec{TO}\|}$$

$$\psi = -T_{\perp} \arccos\left(\frac{\vec{TL}' \cdot \vec{TO}}{\|\vec{TL}'\| \cdot \|\vec{TO}\|}\right)$$

For each scenario, these angles were computed using the specified Sun and Observer positions, considering for each Targets. These calculations provide a detailed geometrical characterization for each Sun-target-observer configuration. Therefore, we can now look at the reflectance behavior for each of this scenarios. The corresponding code can be found in the [geometry.py](#) file.

The following pages showcase all the results for every scenarios created from [Table 1](#).

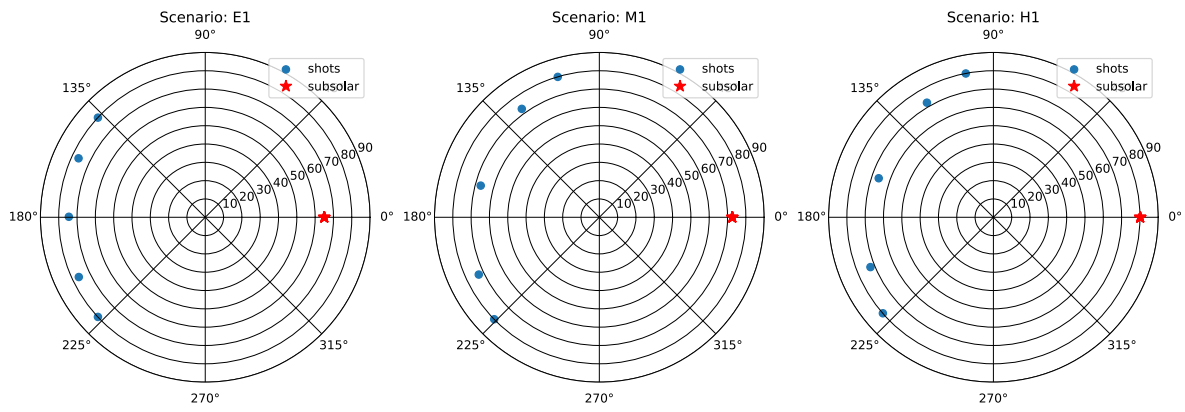


Figure 8: Polar plot of the emergence and incidence over the azimuth

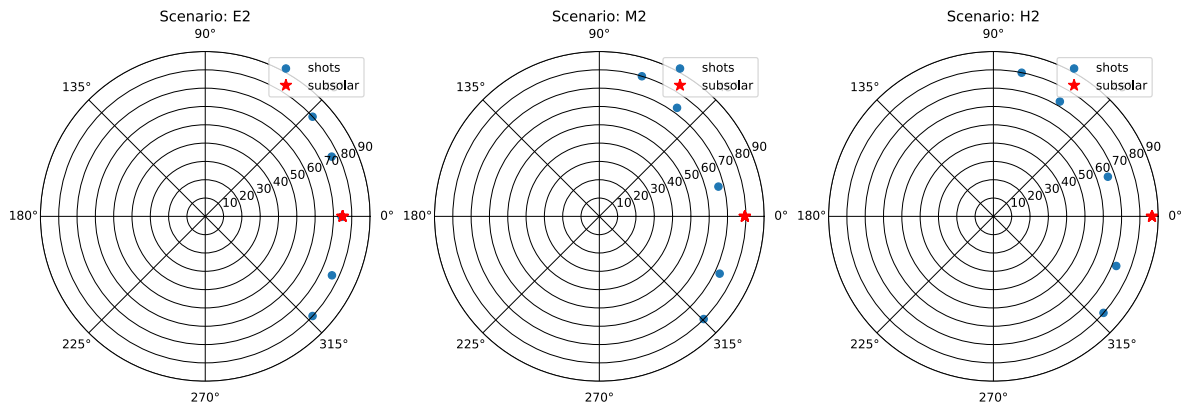


Figure 9: Polar plot of the emergence and incidence over the azimuth

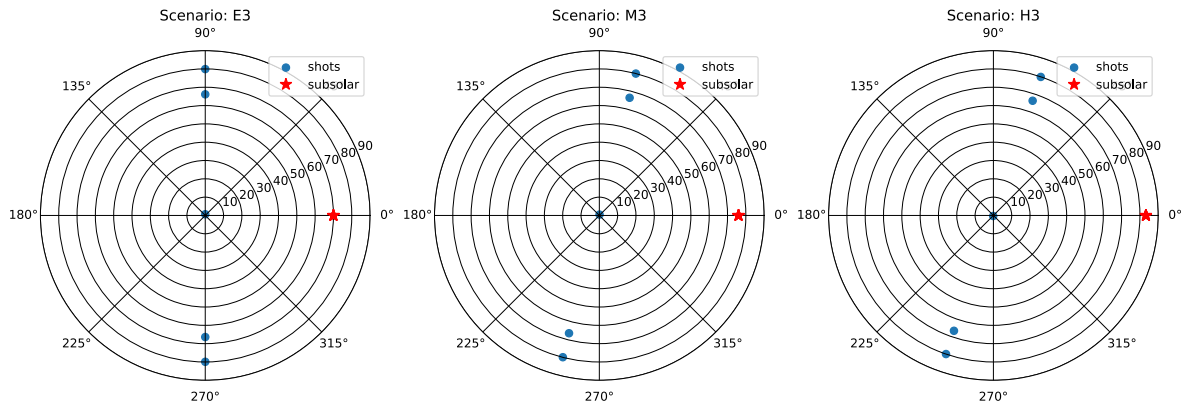


Figure 10: Polar plot of the emergence and incidence over the azimuth

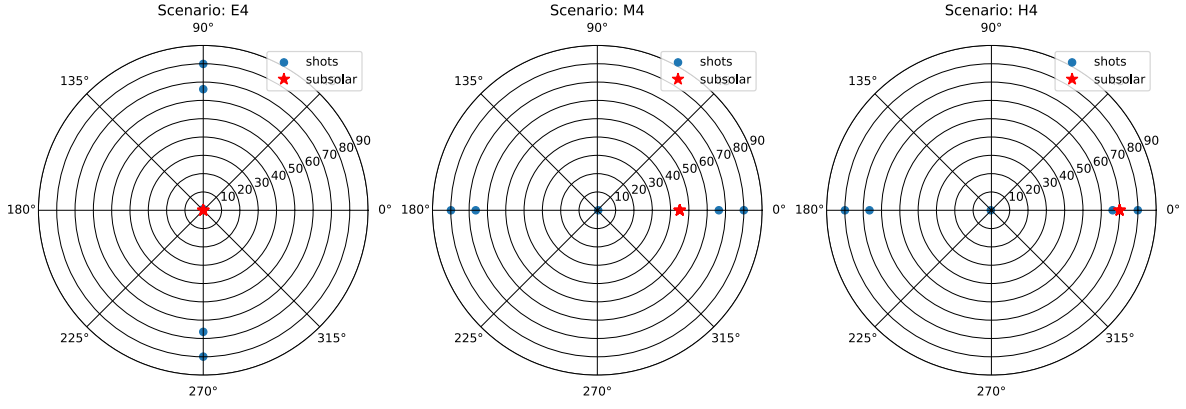


Figure 11: Polar plot of the emergence and incidence over the azimuth

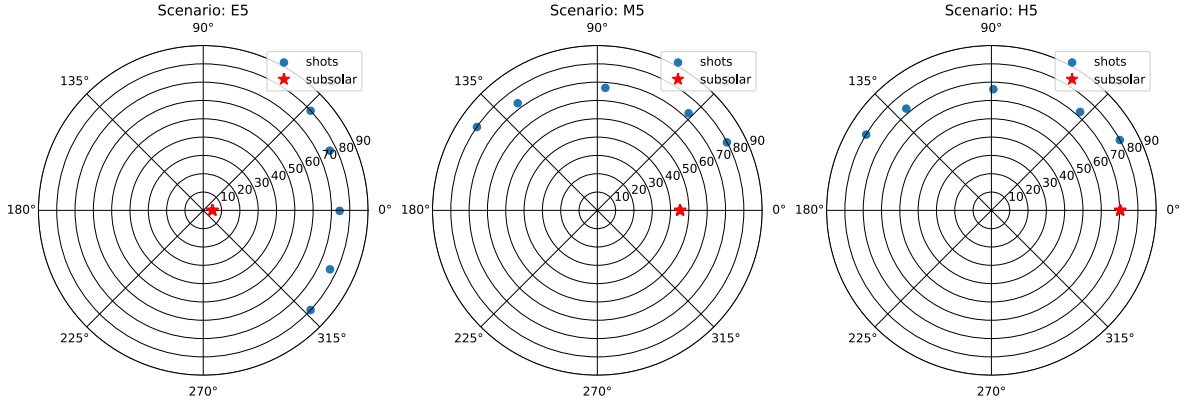


Figure 12: Polar plot of the emergence and incidence over the azimuth

### 2.2.1 Combination of orbit

For each target position case (E, M and H) we could cumulate from one to 5 orbit type. For instance scenario E1, E1-E2, E1-E2-E3, but also all of them E1-E2-E3-E4-E5. There is in total 31 possible combinations of orbit type for each target position. Obviously, it is not possible to combine geometries from target at equator and mid-latitude. Therefore, we are left with 93 total scenarios of combinations possible.

### 3 Creation of multiples set of photometric parameters

#### 3.1 Surface photometry

In each pass over a target region, the satellite captures reflectance measurements under different incidence, emission, and phase angles. These measurements will later be analyzed using the Hapke radiative transfer model [Sat14] to derive photometric parameters that can indicate the microphysical properties of the surface materials. By observing from multiple angles, the mission aims to enhance the understanding of how light interacts with the lunar surface, which provides insight into the geological composition and texture of the observed areas.

From [Fer16] photometric parameters are defined as follow: The single scattering albedo ( $\omega$ ) represents the fraction of incident light scattered by a single particle rather than absorbed, providing insight into the material's reflectivity, with values ranging from 0 (completely absorbing) to 1 (completely scattering). The Hapke mean slope roughness parameter ( $\zeta$ ) quantifies the macroscopic roughness of a surface influencing light scattering and shadowing effects. The opposition effect amplitude ( $B_0$ ) describes the magnitude of the sharp brightness. The asymmetry parameter ( $b$ ) characterizes the angular distribution of scattered light, distinguishing isotropic ( $b = 0$ ), forward-scattering ( $b > 0$ ), and backscattering ( $b < 0$ ) behaviors, while the backscatter fraction ( $c$ ) defines the proportion of light scattered back toward the source, with higher values indicating surfaces with irregular or opaque particles. Lastly, the opposition effect width ( $h$ ) represents how sharply the brightness increases near zero phase angle. The Figure 13 showcase the variety of surface types.

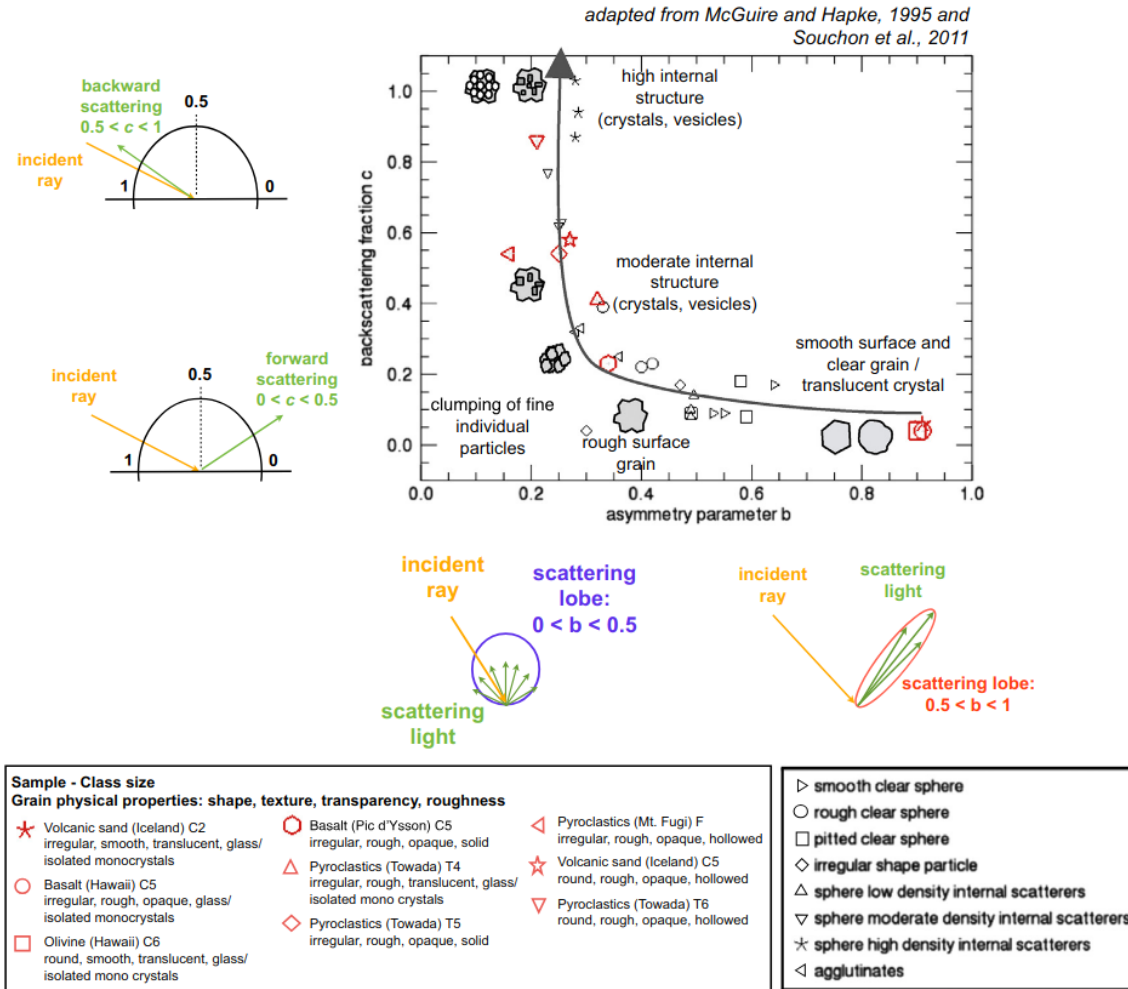


Figure 13: Particle phase function parameter results of the experimental studies from [A M95]

### 3.2 Photometric parameters configurations

We now have multiple orbit scenarios set-up, therefore the next step will focus on defining the behavior of the reflectance for each scenario. For this purpose, photometric parameters needs to be defined for different surface type.

To comprehensively analyze the impact of various surface and illumination properties on reflectance, multiple photometric scenarios were generated by varying key parameters of the Hapke radiative transfer model. These parameters were carefully chosen to cover a wide range of plausible surface conditions. The combinations used in this study are as follows in [Table 2](#):

$\omega$	$b \ \& \ c$	$\zeta$	$b_0$	$h$
0.3	(0.3,0.9)	0	0.5	0.5
0.9	(0.3,0.9)	0	0.5	0.5
0.3	(0.3,0.5)	0	0.5	0.5
0.3	(0.9,0.1)	0	0.5	0.5
0.9	(0.3,0.5)	0	0.5	0.5
0.9	(0.9,0.1)	0	0.5	0.5
0.3	(0.3,0.9)	30	0.5	0.5
0.9	(0.3,0.9)	30	0.5	0.5
0.3	(0.3,0.5)	30	0.5	0.5
0.3	(0.9,0.1)	30	0.5	0.5
0.9	(0.3,0.5)	30	0.5	0.5
0.9	(0.9,0.1)	30	0.5	0.5

Table 2: Summary of all configurations used to analyze photometric responses across different latitudes.

By evaluating these scenarios, we aim to better understand how photometric behavior varies under different microphysical conditions, informing the optimal choice of parameters for the mission’s orbital configurations.

#### 3.2.1 Reflectance calculus

The reflectance is calculated for all possible photometric parameters [Table 2](#) and geometric orbit combinations [Table 1](#). It has in inputs the photometric parameters, incidence, emergence, phase and azimuth angles. The calculus is based on Hapke’s photometric model [[Sat14](#)] and goes through the surface roughness corrections, shadowing effects, multiple scattering effect within particles, the opposition effect and phase function dependence. The result is the bidirectional reflectance of the surface under specified illumination and viewing geometry. This part has for objective to simulate the reflectance received by the satellite, which we will then inverse using the geometric orbit angles to approximate photometric parameters and conclude wether or not the scenario is well suited to approximate the surface photometric parameters.

The corresponding python code can be found it the [main.py](#) file.

## 4 Reflectance inversion to estimate photometric parameters

### 4.1 inversion method

The reflectance can be calculated with the python [MC3](#) (Multi-Core Markov Chain Monte Carlo) library, it is a powerful Python tool for Bayesian parameter estimation and model fitting with great details on the statistic output. It uses the Markov Chain Monte Carlo (MCMC) method to sample the posterior probability distribution of the model parameters. It has features like adaptive step-size tuning and Gibbs sampling [[Cub+17](#)] to ensure that the parameter space is thoroughly explored. MC3 provides detailed results, including posterior distributions, parameter uncertainties, and convergence quality, making it a valuable tool for a statistical analysis.

We used the sample function from the MC3 library, requiring in entry the reflectance measured and it's uncertainties, the reflectance calculus function from the [subsubsection 3.2.1](#) with it's accompanying arguments and finally the initialization parameters for the algorithm in it self. The sample function returns multiple very interesting results such as , the best parameters fit, the thinned posterior distribution, the  $X^2$  values for the posterior samples, the mean of the marginal posteriors for each model parameter and the standard deviation of the marginal posteriors for each model parameter.

To simulate real-world measurement, a "noised" version of the reflectance data is generated. This step mimics potential observational inaccuracies, adding a realistic element to the simulated data, see [inversion.py](#) ([l10:13](#)). The corresponding python code for the uses of the inversion function can be found in the [main.py](#) file.

The following [Figure 14](#) and [Figure 15](#) showcase the given results from the inversion method. To evaluate the quality of the inversion algorithem over the true parameters, we refined the thinned posterior distribution by excluding the burn-in phase and filtering out unwanted data, ensuring that the goodness-of-fit metric between the model and the observed data was limited to values less than 30, see [code](#). This allow us to get only the final converged results that can be quantified and estimated, later used in [compare.py](#) and [subsubsection 4.1.1](#). The following [Figure 14](#) represents all the reflectance values over the phase for all shots of the scenario, here we have the combination of the orbit E1, E2, E3, E4, and E5 for  $\omega = 0.9$ ,  $b = 0.3$ ,  $c = 0.9$ ,  $\zeta = 30$ ,  $b_0 = 0.5$ ,  $h = 0.5$ , with 5 shots per orbit.

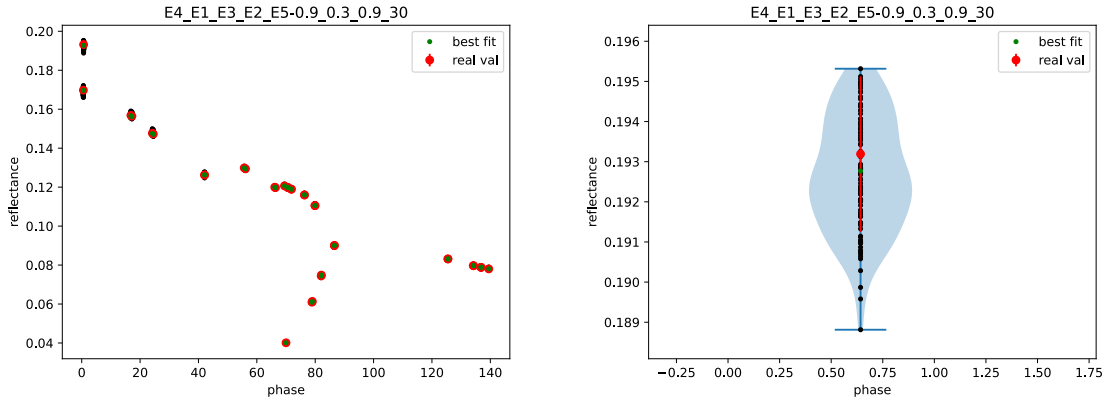


Figure 14: Polar plot of the emergence and incidence over the azimuth



The following figure represents the thinned posterior distribution, without the burn-in phase delimited where the chisq output is  $> 30$ . The red colored point represents the true parameter value with its uncertainties  $\epsilon$  area and the green colored point represents the best fitting output parameter from the Hapke model. Consequently, this figure showcase the convergence quality of the model past the threshold physq value  $< 30$ . This corner graph greatly exhibit co-relation between photometric parameters, indeed it is a great tool to quickly see if a combination of geometry and photometry works well together.

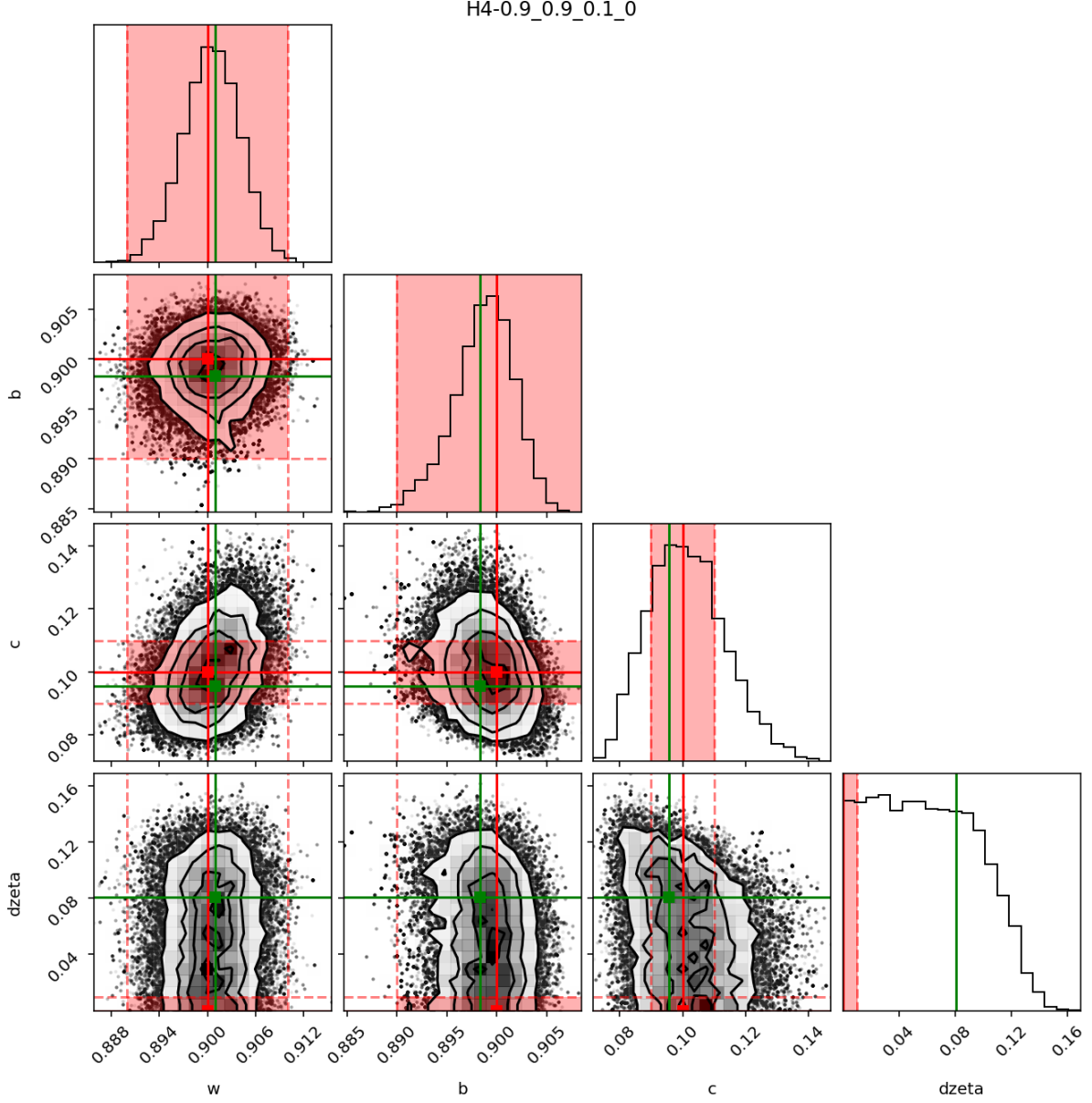


Figure 15: Polar plot of the emergence and incidence over the azimuth

This led us to the next chapter [subsubsection 4.1.1](#) dedicated to the estimation of the geometric configuration quality explained by [Sch19]

#### 4.1.1 Estimation of the geometric configuration quality

The geometric configuration quality can be expressed numerically by considering the MC3 output parameters  $\omega'$ ,  $b'$ ,  $c'$ ,  $\zeta'$ ,  $B'_0$ , and  $h'$  resulting from the noised reflectance and orbit geometric angles. As explained by [Sch19] The closer the solution to the true parameter set is, the better the estimate. We measure the quality of the tested geometry by considering, for every parameter (for example  $\omega'$ ), the part of the distribution  $\sigma(\omega')$  which lies inside the interval  $[\sigma(\omega') - \epsilon, \sigma(\omega') + \epsilon]$ , where  $\epsilon$  is set to 1% and 2.5% of the total parameter space. We consider:

$$I = \begin{pmatrix} \omega \\ b \\ c \\ \zeta \end{pmatrix}, \quad D = -\log(I)$$

Therefore  $D_\omega$  decreases with  $I_\omega$  and so on for all parameters, it is equals to 0 when the full distribution  $\sigma(\omega)$  lies inside the interval of interest  $[\sigma(\omega') - \epsilon, \sigma(\omega') + \epsilon]$  and equals  $+\infty$  if  $\sigma(\omega) = 0$  in  $[\sigma(\omega') - \epsilon, \sigma(\omega') + \epsilon]$ . Quantities  $D_b$ ,  $D_c$ ,  $D_\zeta$ ,  $D_{B_0}$  and  $D_h$  are defined similarly. The total efficiency distance  $E$  of a given geometry is finally defined by the sum:

$$E = D_b + D_c + D_\zeta$$

From the  $N_{\text{samp}}$  samples obtained via the MCMC procedure, we consider the best fit, noted  $\tilde{n}$  that yields the minimum chi-square value  $X^2$ , with:

$$X^2 = \sum_i \frac{r_i - r_{l,i}}{\sigma_i^2}$$

which equivalently corresponds to the maximum likelihood with  $r_{l,i}$  being the reflectance vector obtained by computing the Hapke model with a set parameters  $m = (\omega, b, c, \zeta, B_0, h)$ . By looking at all scenarios we can establish for each type (E,M,H) and for each number of orbit in a scenario the best scenario.

Scenario	$X^2$ Value
E2	10.322
E2 + E3	4.581
E1 + E2 + E3	3.491
E1 + E2 + E3 + E4	2.903
E1 + E2 + E3 + E4 + E5	2.906
M4	5.819
M3 + M4	3.690
M1 + M3 + M4	3.223
M1 + M3 + M4 + M5	3.004
M1 + M2 + M3 + M4 + M5	2.830
H4	5.2808
H2 + H4	3.081
H2 + H3 + H4	2.523
H2 + H3 + H4 + H5	2.249
H1 + H2 + H3 + H4 + H5	2.165

Table 3: Summary of all configurations used to analyze photometric responses across different latitudes.

## 5 Results

### 5.1 Results on one orbit

## 5.2 Results on combination of orbit

The following Figure 16 represents the total efficiency  $E$  of each Equatorial scenarios, the lower the value the better the scenario is. On Figure 16 sides bargraph represents the mean values for each geometry on top and mean values combined with the standard deviation on the right for each photometry.

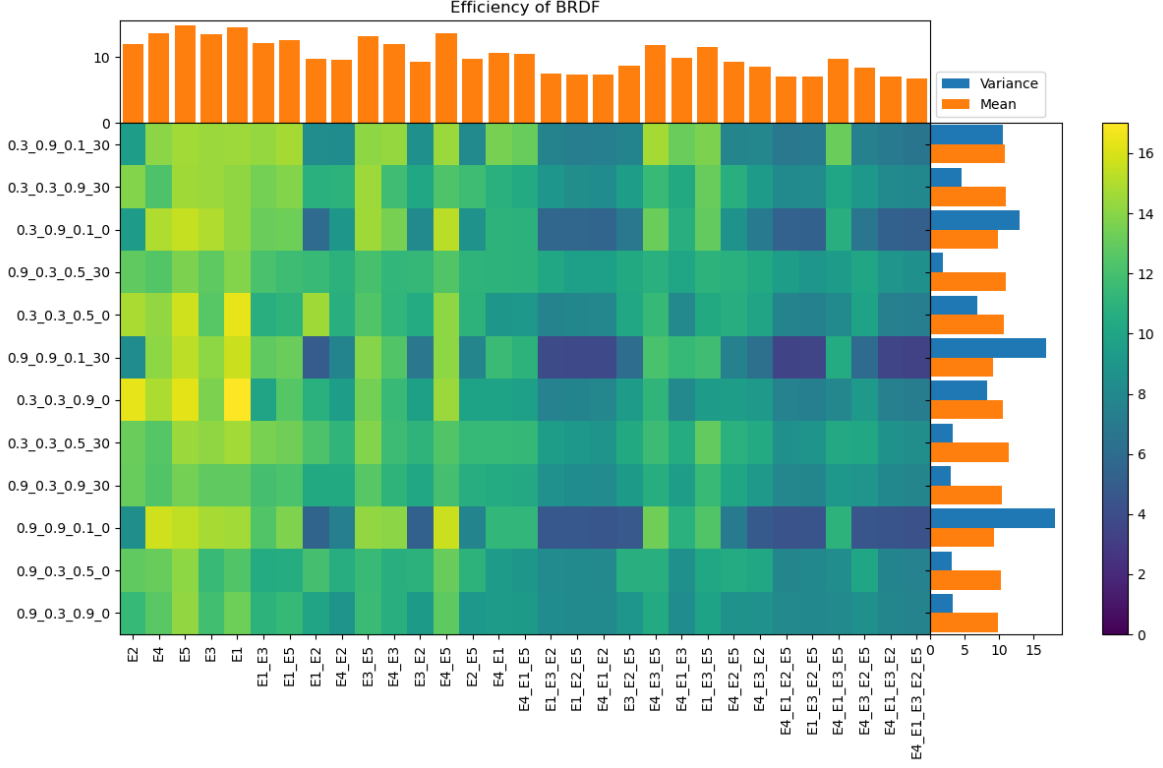


Figure 16: Heatmap of the efficiency values for each geometry and photometry at the equator, with mean values displayed at the top and variance values on the right.

We can see from the Figure 16 all the best geometry combinations per type and per number of revolutions, with their mean efficiency values displayed at the top. These values clearly highlight which BRDF geometries perform best on average. The heatmap reveals interesting behavior, where the choice of geometry strongly influences the inversion results. Certain configurations produce high efficiency (lighter regions), while others perform poorly (darker regions), indicating a strong dependence of the BRDF inversion process on the selected angular geometry and photometric model. Additionally, the variance values shown on the right provide insights into the consistency of each geometry's performance. Geometries with high variance exhibit inconsistent results, while those with low variance are more robust and reliable. Notably, lower revolution counts generally achieve better efficiency, particularly for models M1 and M2, suggesting that simpler angular configurations yield more reliable inversion results. This sensitivity to geometry highlights the importance of careful selection and optimization of angular configurations to improve both efficiency and stability in BRDF inversion.

The following Figure 17 represents the total efficiency  $E$  of each medium latitude scenarios, the lower the value the better the scenario is. On Figure 17 sides bargraph represents the mean values for each geometry on top and mean values combined with the standard deviation on the right for each photometry.

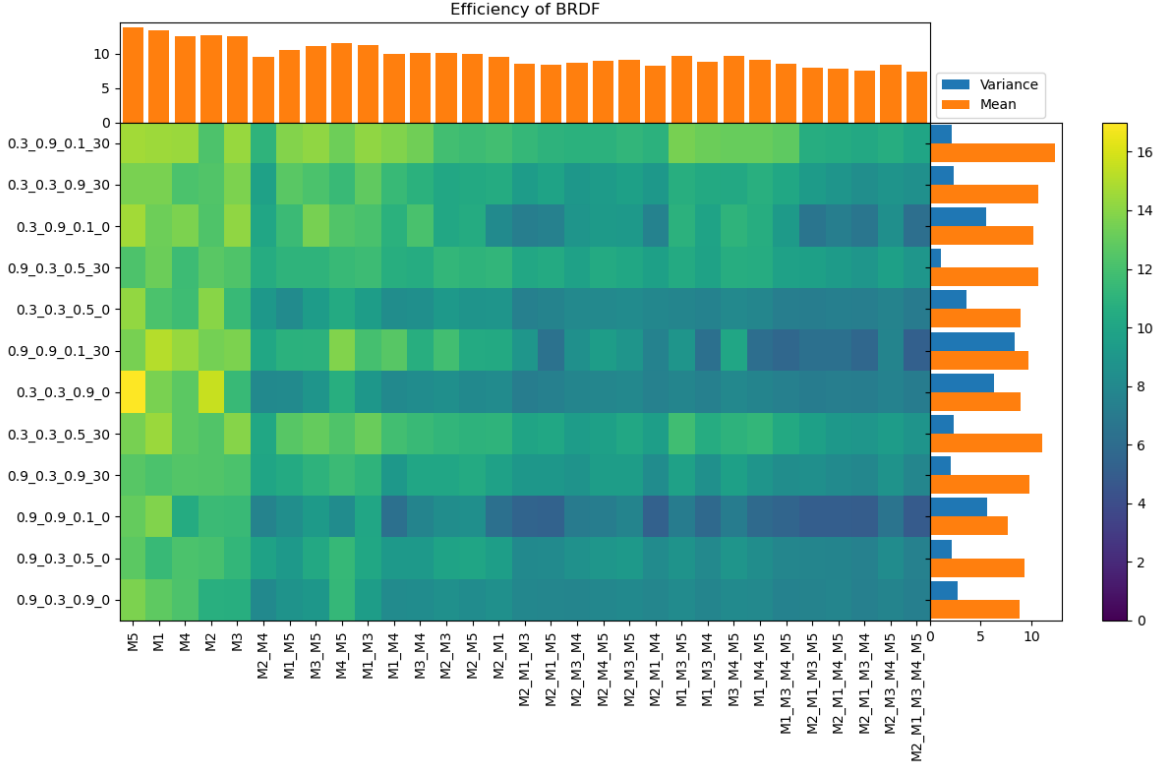


Figure 17: Heatmap of the efficiency values for each geometry and photometry at the equator, with mean values displayed at the top and variance values on the right.

about

The following Figure 18 represents the total efficiency  $E$  of each high latitude scenarios, the lower the value the better the scenario is. On Figure 18 sides bargraph represents the mean values for each geometry on top and mean values combined with the standard deviation on the right for each photometry.

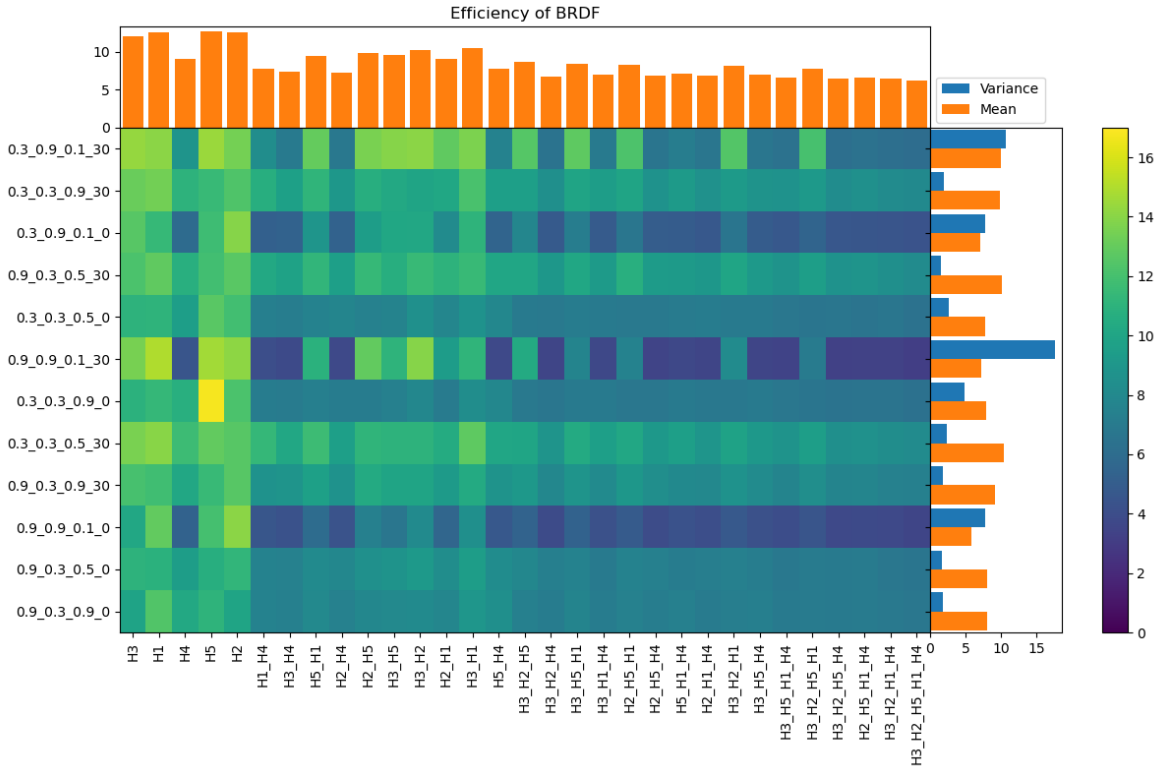


Figure 18: Heatmap of the efficiency values for each geometry and photometry at the equator, with mean values displayed at the top and variance values on the right.

about

### 5.3 Effect of the noise level